Research Square

Preprints are preliminary reports that have not undergone peer review.
They should not be considered conclusive, used to inform clinical practice,
or referenced by the media as validated information.

Solute-Driven Defect Engineering in a Tungsten‐Based High‐Entropy Alloy for Extreme Radiation Tolerance

jianlong Chai
Dahuan Zhu
1207695690@qq.com

Junling Chen

Research Article

Keywords: W-based HEAs, Helium bubble suppression, Defect‐solute interaction, Dislocation loop tailoring, Chemical disorder, Atomistic simulation

Posted Date: February 26th, 2026

DOI: https://doi.org/10.21203/rs.3.rs-8952179/v1

License: This work is licensed under a Creative Commons Attribution 4.0 International License.
Read Full License

Additional Declarations: The authors declare no competing interests.

Solute-Driven Defect Engineering in a Tungsten-Based High-Entropy Alloy for Extreme Radiation Tolerance

Jianlong Chai[1,2], Dahuan Zhu[3*], Junling Chen[3]

[1] School of Nuclear Science and Technology, University of Science and Technology of China, Hefei 230026, People's Republic of China
[2] Institute of Modern Physics, Chinese Academy of Sciences, Lanzhou 730000, People's Republic of China
[3] Institute of Plasma Physics, HFIPS, Chinese Academy of Sciences, Hefei 230031, China

Abstract

Fusion energy demands materials that withstand extreme helium irradiation, a challenge that conventional tungsten fails to meet due to bubble embrittlement and hardening. Here we report a WTaVCr high-entropy alloy (HEA) in which chemical disorder fundamentally alters helium-defect dynamics. Through ion irradiation, atomic-scale microscopy, and atomistic simulations, we uncover a unique solute-defect interplay that suppresses degradation. Unlike pure tungsten, the HEA retains nanometer-scale helium bubbles (~1 nm) without coarsening as the He fluence increases. Dislocation loops in the alloy showing an increasing fraction of <100>-type loops accompanied by Cr enrichment and Ta depletion at loop interfaces. Atomic-scale analysis and simulations unveil a thermodynamically driven segregation process where Cr enriches at dislocation loops while Ta is excluded, a direct result of atomic size mismatch and strain minimization. Nanoindentation reveals quantifiable hardening governed by loop density and character. These results demonstrate that configurational entropy alone is insufficient; deliberate solute-dislocation interactions are critical for defect control. By linking chemical heterogeneity to microstructural evolution, this work provides a design principle for alloys that maintain mechanical integrity in high-radiation environments, paving the way for durable fusion materials.

Keywords: W-based HEAs; Helium bubble suppression; Defect-solute interaction; Dislocation loop tailoring; Chemical disorder; Atomistic simulation

Corresponding author.
Email address: dhzhu@ipp.ac.cn;

1. Introduction

Tungsten (W) stands out as a prime contender for the divertor or plasma-facing materials (PFMs) in upcoming fusion reactors, thanks to its elevated melting point, excellent thermal conductivity, minimal sputter yield, and low tritium retention [1][2]. Despite these benefits, W is plagued by inadequate mechanical properties stemming from its low fracture toughness and high ductile-to-brittle transition temperature (DBTT). These limitations severely constrain its operational temperature range. Nevertheless, when exposed to irradiation, tungsten undergoes significant microstructural alterations that ultimately impact its thermal and mechanical properties. For example, under irradiation from He ions generated by fusion neutrons, substantial morphological changes can occur on the surface of W. These alterations may involve the formation of nanoscale bubbles and low-density fuzz structures [3][4]. The adverse effects have significantly hindered the application of W in fusion reactors. Hence, several approaches have been suggested and explored to enhance the performance of tungsten. These primarily involve incorporating minor dopant elements or adjusting its microstructure [5]. Adding different alloying elements (such as W-Re and W-Ti) or engineering the nanostructure of W are considered common strategies to enhance the processing and operational performance of materials. Based on the latter strategy, recent studies indicate that advanced nanocrystalline tungsten samples have formed numerous He bubbles at grain boundaries, leading to adhesion loss and inferior mechanical properties at operating temperatures, thereby diminishing their applicability in fusion environments [6][7]. Consequently, the development of novel material systems is crucial for making nuclear fusion a viable energy source. The emergence of HEAs offers an alternative robust method to adjust alloy characteristics by manipulating chemical disorder. HEAs are intricate metallic compounds comprised of multiple elemental components, each present in high concentrations [8][9]. Due to the pronounced configurational entropy inherent in their composition, these alloys commonly crystallize into fundamental face-centered cubic (FCC) or body-centered cubic (BCC) structures. Within HEAs, the atomic environment surrounding each atom is unique, resulting in variances in defect properties even within the same material. Noteworthy is the observation that defect energies, encompassing formation and migration energies, exhibit statistical distributions [10]. This phenomenon potentially intensifies the interaction between vacancies and interstitials, thereby bolstering defect recombination and, consequently, enhancing irradiation resistance [11].

Certainly, recent experimental findings have showcased exceptional radiation durability in W-based HEAs. Take, for instance, the $W_{38}Ta_{36}V_{11}Cr_{15}$ HEAs of single BCC phase exhibits no indication of dislocation loops resulting from irradiation with 1 MeV Kr^{2+} up to a dose of 8 displacement per atom (dpa) at 1073 K [12]. Zhao et al. [9] calculated the defect properties in a WTaVCr equiatomic HEA with BCC structure using first-principles. In comparison to FCC HEAs, the BCC HEAs demonstrates significantly larger overlap regions in the distribution of migration energies for vacancies and interstitials. This characteristic enhances defect recombination,

contributing to its superior irradiation resistance. El-Atwani et al. [13] investigated the response of nano-crystalline WTaVCr HEA under low-energy He injection at 1223 K. The results indicate that the alloy tends to form uniformly distributed small bubbles. Similar to high-energy irradiation, the response of this alloy to He injection is significantly superior to pure nano-crystalline W and other studied alloys (such as W-TiC). Kalita et al. [14] investigated the He^+ ion irradiation resistance of the WTaVCr HEA film at room temperature and found that with the increase in the injection of He^+ ions, the density of bubbles increases, while the size of the bubbles remains constant.

While low-activation WTaVCr HEA are seen as a substitute for W in PFMs, there is limited data available regarding the effects of He^+ ion irradiation on the performance of these alloys, particularly concerning the evolution of irradiation-induced defects and mechanical properties. Considering this, the primary objective of the presented study was to assess the resistance of WTaVCr HEA compared to W against the evolution of defects induced by helium and the associated changes in mechanical properties during He+ ion irradiation.

2. Materials and methods

2.1. Materials

High-purity raw materials (W-99.95%, Ta-99.95%, V-99.9%, Cr-99.9%) were used to fabricate the WTaVCr HEA via vacuum arc (Model YC-20160024). Prior to melting, the furnace chamber was evacuated to 3 mbar and then backfilled with Ar (purity, 99.998 vol.%). The alloy ingots were processed into 5×5×1 mm^3 flakes and polished to a mirror surface for ion irradiation experiment. The density of the irradiated sample was determined to be 12.08 g/cm^3. The X-ray diffraction (XRD) pattern of the WTaVCr HEA is presented in Fig. 1a, confirming its single-phase BCC structure. Elemental mapping performed via energy-dispersive spectroscopy (EDS) further reveals a homogeneous distribution of all constituent elements.

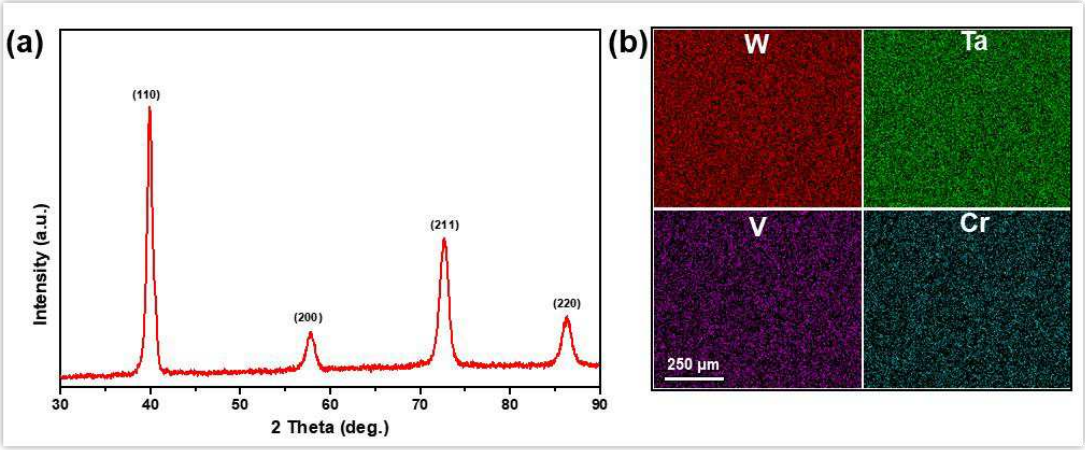


Fig. 1 (a) XRD pattern of the unirradiated WTaVCr HEA. (b) The elemental distribution in the WTaVCr HEA from STEM-EDS.

2.2. Ion irradiation experiment

The 270 keV He^+ ion irradiation was primarily conducted at the terminal chamber of the ECR source's 320 kV high-voltage platforms at the Institute of Modern Physics, Chinese Academy of Sciences, in Lanzhou, China. The irradiation was carried out with fluences ranging from 7.5E16 to 3.2E17 ions/cm^2 at temperatures of 500°C and 800°C. The He^+ ion beam was oriented perpendicular to the sample surface in a vacuum of less than 10^-4 Pa. The irradiation damage was computed using the quick Kinchin-Pease calculation mode in SRIM 2013 [15]. The threshold displacement energy for the elements of W, Ta, V, Cr were set as 90, 90, 57 and 40 eV, respectively [16], and the depth profiles of atomic displacement damage calculated was plotted in Fig. 2. The results showed that the peak damage (~600 nm) and He concentration at 7.5E16 ions/cm^2 were 1.1 and 4.0 at.%, respectively.

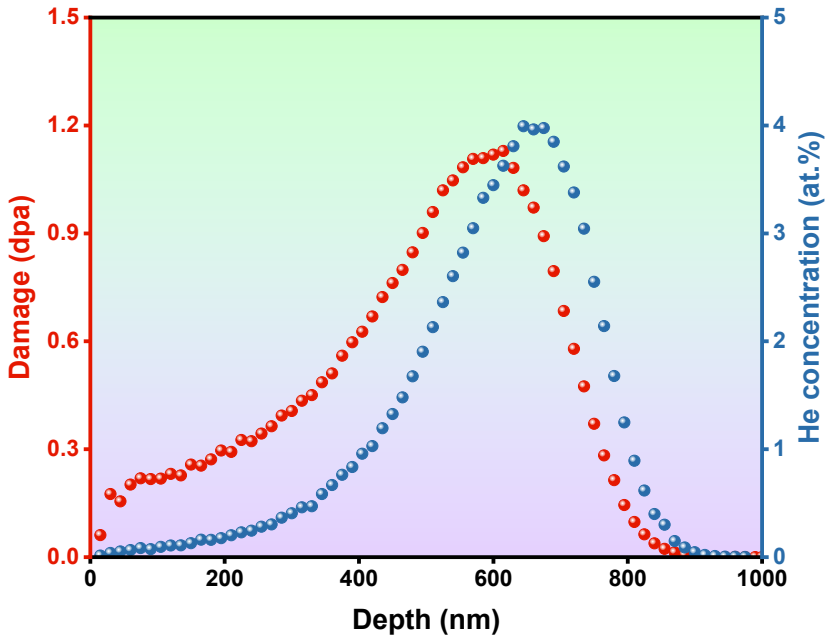


Fig. 2 Depth distribution of dpa and He concentration calculated by SRIM in WTaVCr HEA irradiated with 270 keV He ions at $7.5\times^{16}$ ions/cm^2.

2.3. Characterization

Thin foil thickness was prepared using a focused ion beam (FIB, Helios SCX), and the thickness of the obtained foils was measured to be ~60 nm via high energy-resolution electron energy loss spectroscopy (EELS). In order to get an ultra-thin and clean sample for TEM characterization, a flash polishing technique was performed to remove the damage introduced by FIB [17]. TEM observations were conducted using the Talos F200X. Nanoindentation techniques (KLA-Tencor Nano Indenter G200) are used to evaluate the nanohardness of irradiated layers. Following the method described by Oliver and Pharr [18], the diamond Berkovich indenter is used in combination with the continuous stiffness measurement (CSM) method to

achieve the measurement of nanohardness. The nanoindentation was carried out at 15 test points for each sample, with 50 μm spacing between indentations. Nanohardness measurements were taken from the point of contact with the nanoindenter to a depth of approximately 1000 nm. The indenter geometry was calibrated using fused silica at a similar indentation depth. It is important to note that the nanohardness of irradiated specimens reflects a composite hardness due to the combined effects of the damage gradient effect (DGE), the indentation size effect (ISE), and the softer substrate effect (SSE) [19][20]. The DGE results from the non-uniform distribution of irradiation-induced defects throughout the specimen's depth. The ISE indicates that indentation hardness varies with indenter size, with greater hardness observed at shallow depths compared to deeper ones. Nix and Gao [21] developed a model based on geometrically necessary dislocations (GNDs) to explain the ISE:

$$H = H_0\sqrt{1+\frac{h^*}{h}} \tag{1}$$

Where H denotes the hardness, H_0 represents the bulk equivalent hardness at an infinite depth, h^* signifies the characteristic depth unique to the specific indenter and material, and h refers to the indentation depth.

Microstructural and microchemical characterization focused on the peak damage regions to minimize artifacts from surface sinks [22][23].

3. Results

3.1 He bubbles

In order to more conveniently compare the size and density of He bubbles, the damage peak region (600-630nm from the surface) is selected as the main observation region shown in Fig. 3. It can be seen, in the four irradiated samples, He bubbles are distributed randomly and uniformly, and there is no obvious normal distribution of bubble size, which indicates that the nucleation and growth process of He bubbles are uniform. With the increase of He concentration, the number density of He bubbles increased, and the size did not change significantly. With the increase of temperature, the number density of He bubbles decreases and the size increases slightly.

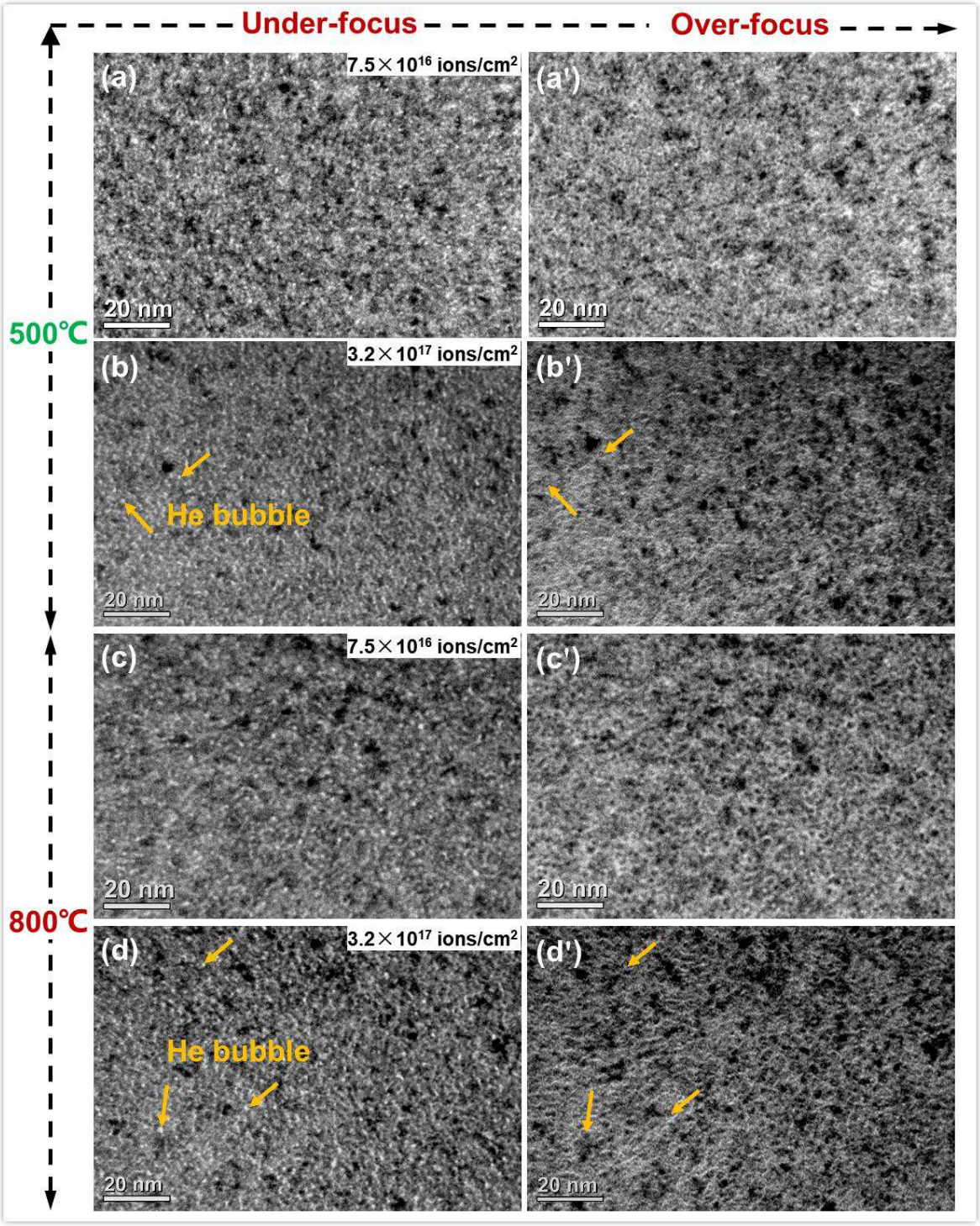


Fig. 3 BF-TEM images of He bubbles formed in He^+ irradiated with changing the damage fluence and the temperature in WTaVCr HEA. (a-d) Underfocus image and (a'-d') Overfocus image were captured for a defocus of 800 nm.

Fig. 4 shows the size distribution and number density of He bubbles in the He damage peak region of WTaVCr alloy. It was observed that the average size and number density of He bubbles increased at all temperatures as expected with the increase of damage. When irradiated at 500 °C to a fluence of 7.5×10^{16} ions/cm^2, the sample exhibited He bubbles with an average size of 0.86 ± 0.28 nm and a number density of 1.43×10^{24} m^{-3}. Under the same temperature but with a fluence of 3.2×10^{17} ions/cm^2, the bubble size and density increased to 0.96 ± 0.21 nm and 2.04×10^{24} m^{-3},

respectively. At 800 °C with a fluence of 7.5×10^{16} ions/cm^2, the average bubble size was 1.02 ± 0.36 nm, with a corresponding density of 1.06×10^{24} m^{-3}. When the fluence was raised to 3.2×10^{17} ions/cm^2 at this temperature, the number density further increased to 1.54×10^{24} m^{-3}, while the average bubble size reached 1.08 ± 0.38 nm. The comparison of the size and number density of He bubbles shows that the effect of temperature and damage on the growth of He bubbles in WTaVCr HEA is not obvious in this work. In pure W, under the same irradiation parameters as in this study, the size of the He bubbles is 1.1 - 2.1 nm [24].

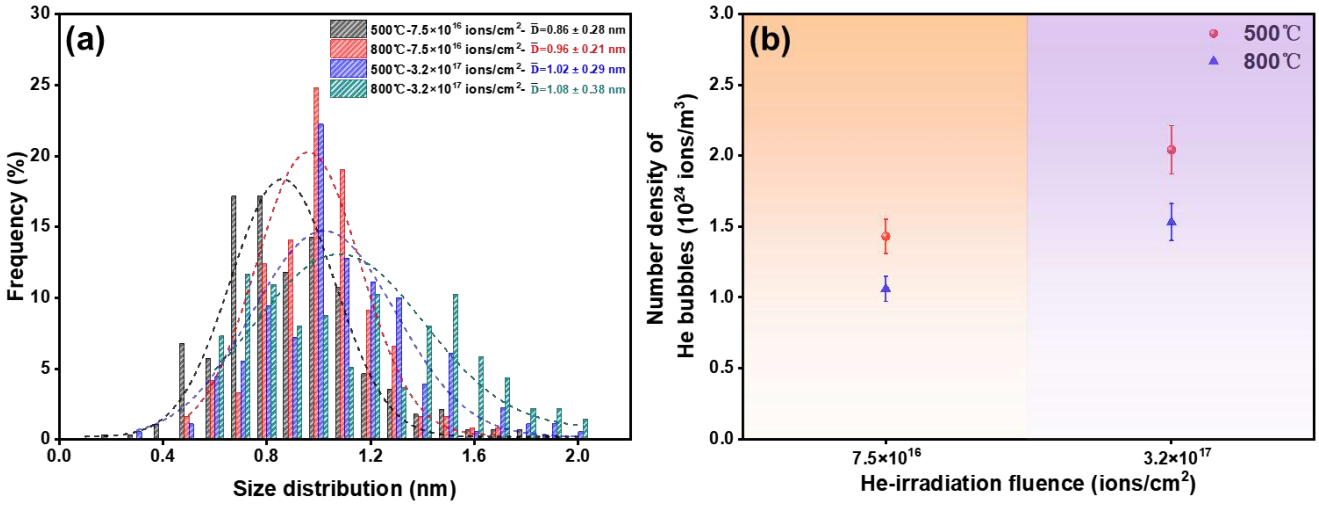


Fig. 4 Average size distribution (a) and number density (b) of He bubbles.

3.2 Dislocation loop

Fig. 5 presents the distribution of the dislocation of all investigated samples around their peak damage regions. The micrographs, taken under strong two-beam conditions using a diffraction vector $\boldsymbol{g}_{110}$ and $\boldsymbol{g}_{200}$ near [001] zone axes, and illustrate the Burgers vectors of dislocation loops by using $\boldsymbol{g}\cdot\boldsymbol{b}=0$. The defects can be clearly observed by comparing the BF-TEM and DF-images, and show that the microstructure consistently consists of small point defects, dislocation loops with minimal or no line dislocations.

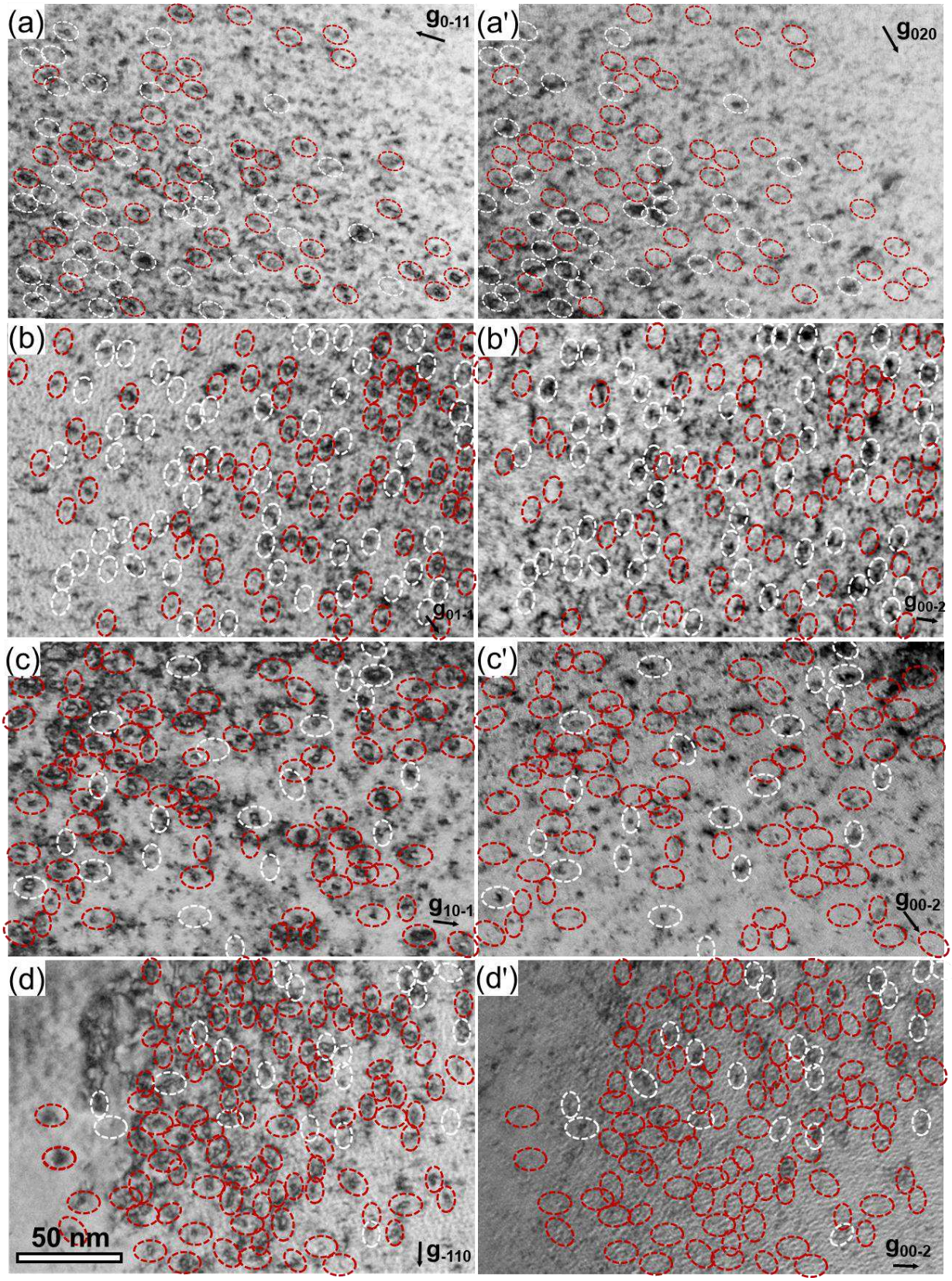


Fig. 5 The Burgers vectors of dislocation loops near the [001] zone axis was determined using the $\boldsymbol{g}\cdot\boldsymbol{b}= 0$ invisibility criterion. For this analysis, two-beam condition TEM images were obtained with $\boldsymbol{g}_{110}$ and $\boldsymbol{g}_{200}$ diffraction vectors from samples irradiated at different fluences. (a) 500℃-7.5×10^{16} ions/cm^2, (b) 500℃-3.2×10^{17} ions/cm^2, (c) 800℃-7.5×10^{16} ions/cm^2, and (d) 800℃-3.2×10^{17} ions/cm^2, respectively.

Quantized size and number density around their peak damage regions were measured, and the statistical results are illustrated that. the mean size and average number density of observed <111> and <100> dislocation loops were determined to be 1.14 nm, 1.14 × 10^{23} /m^3, 1.27 nm, 0.90 × 10^{23} /m^3 for 500℃-7.5×10^{16} ions/cm^2, 1.91 nm，0.69 × 10^{23} /m^3, 1.62 nm, 1.42 × 10^{23} /m^3 for 500℃-3.2×10^{17} ions/cm^2, 1.93 nm，0.40 × 10^{23} /m^3, 1.88 nm, 1.08 × 10^{23} /m^3 for 800℃-7.5×10^{16} ions/cm^2, and 2.88 nm, 0.38 × 10^{23} /m^3, 1.86 nm, 1.12 × 10^{23} /m^3 for 800℃-3.2×10^{17} ions/cm^2, respectively. Therefore, according to the $N = {}^{2}/_{3}N_{<100>}+{}^{1}/_{2}N_{<111>}$, the densities of dislocation loops in the alloy under the four sets of parameters are as follows: 1.17, 1.27, 0.92 and 0.94 × 10^{23} /m^3. Evolution of dislocation loop number density from 500℃ to 800℃ in alloys are similar to the evolution of He bubbles that increase in size and decrease in density.

3.3 Nanohardness

Fig. 6(a) shows the relationship between averaged nanoindentation hardness (H_{NI}) values and indentation depths (h) for both unirradiated and irradiated samples. The mean H_{NI} values decrease steadily with increasing indentation depth up to 1000 nm, attributed to the indentation size effect (ISE). Fig. 6(b) depict the relative hardening, calculated as (H_{Irr}/H_{Unirr} - 1), where H_{Irr} and H_{Unirr} are the mean hardness values at the indentation depth for irradiated and unirradiated specimens, respectively. Due to factors like indenter sharpness, specimen surface flatness, and testing conditions [25], data from the first 120 nm were considered unreliable. Therefore, only data from depths greater than 120 nm were used. Between 120 nm and about 220 nm, relative hardness increased sharply, then decreased gradually from 220 nm to 1000 nm. The rise in relative hardening between 120-220 nm is mainly due to increased displacement damage with depth. To determine the bulk equivalent hardness of the surface layers for both types of specimens (indicated by dashed lines), profiles were plotted using formula (1) based on the square of the nanoindentation hardness (H_{IN}^2) and the reciprocal of indentation depth (1/h), as shown in Fig. 6(c). It is worth noting that H_{NI}^2 and 1/h of isochronously annealed samples basically show a single linear relationship, and the curves of irradiated samples show bilinear characteristics, and the curves bend downward at 220 ~ 1000 nm, reflecting the soft substrate of unirradiated samples. The (H_{NI}^2 - 1/h) profiles for the irradiated samples show varying slopes at different depth intervals, indicating that the composite hardness is influenced by both the irradiated layer and the substrate at different stages of deformation.

Based on the data from Fig. 6(b) and 6(c), the intrinsic hardness (H_0) of the unirradiated and irradiated samples was assessed by fitting data within the depth range of 120 to 220 nm. Fig. 6(d) displays the value of H_0, along with the irradiation-induced hardness increment ($\Delta H_0^{\mathrm{irr}} = H_0^{\mathrm{irr}} - H_0^{\mathrm{unirr}}$). As He concentration increase, the material's hardness progressively improves, with a notably greater hardening effect seen after irradiation at 800°C.

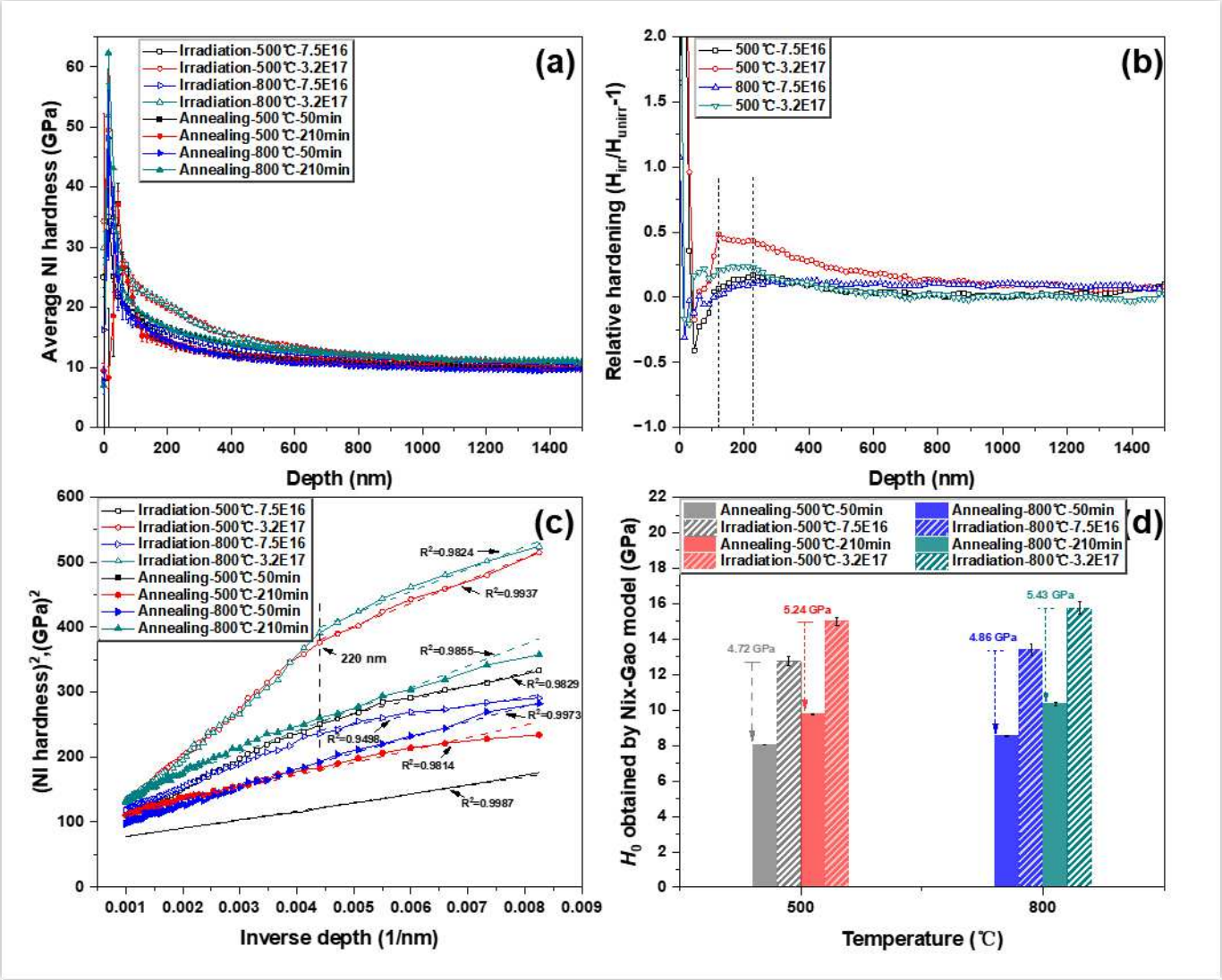


Fig. 6 The average hardness profiles of (a), the corresponding profiles of relative hardening (H_{Irr}/H_{Unirr} −1) (b), and (H_{NI})^2 -1/h profile of unirradiated and irradiated WTaVCr for (c), and (d) H_0 calculated by the Nix-Gao model for the indentation depth (120 nm < h <220 nm).

4. Discussion

4.1 Evolution of He bubbles

According to the analysis of the results, WTaVCr HEA has smaller He bubble than pure W, and these sizes do not change significantly with the accumulation of irradiation damage. Therefore, it is essential to determine the source of the high radiation resistance to helium bubble formation in HEAs. Becquart et al. [26] demonstrated that the average formation energy of interstitial He in the alloy is ~2 times lower than the formation energy in pure W. El-Atwani et al. [13] also note the presence of sites with low formation energy that are likely to create deep wells in the potential energy landscape, acting as strong traps for helium and potentially impeding its migration. In BCC metals, He can occupy two types of interstitial sites: octahedral (OIS) and tetrahedral (TIS). For WTaVCr, the TIS is more energetically favorable for

He than the OIS, aligning with observations in WTaVCr [27]. Thus, only the TIS will be considered in the following analysis. Although WTaVCr features multiple TISs, the solution energies of helium at these sites range from 3.35 to 5.39 eV, which are notably lower than those in W [28][29]. This indicates that helium dissolution in WTaVCr is significantly easier than in tungsten, resulting in much lower helium trapping energies in a single vacancy in WTaVCr compared to W. Zhai et al. [30] propose that the aggregation of helium in WTaVCr is additionally driven by the electrophobic mechanism. Their results indicate that while helium is more prone to dissolve in WTaVCr, its self-trapping ability is considerably reduced, which suggests a suppression of helium bubble nucleation and growth. Based on classical nucleation theory [31], they argue that although helium clusters have positive clustering energy, nucleation in WTaVCr still requires additional energy to overcome an activation energy barrier. This differs significantly from tungsten, where the nucleation free energy decreases steadily with cluster size, suggesting spontaneous helium cluster formation. As a result, spontaneous nucleation of helium clusters may be suppressed in WTaVCr, leading to smaller helium bubbles in WTaVCr compared to those in tungsten, as observed experimentally. Furthermore, the binding energy of helium with He-vacancy complexes in WTaVCr is significantly lower than in pure W, which further inhibits the growth of He-vacancy complexes. In addition, the diffusion energy barrier for a helium atom in HEAs is higher compared to traditional metals, which is one of the possible reasons why HEAs inhibits He bubbles [32].

Increasing the He^+ ion fluence resulted in a higher bubble density, while their size remained relatively unchanged. This observation is consistent with the findings of Kalita [14], who reported that with an increase in He^+ ion fluence, the bubble density rose, but the bubble size stayed constant. Notably, their study was conducted at room temperature. This suggests that the accumulation of He occurs primarily through the nucleation of new He bubbles, rather than through the expansion of existing ones. This behavior may be linked to increased defect recombination or a reduction in the mobility of He within multicomponent alloys. As the temperature increases, the migration rate of He in the HEA structure rises, but the bubble size does not show a significant increase. This confirms that WTaVCr HEA exhibit superior resistance to Helium irradiation compared to pure W or other tungsten-based composites. This phenomenon could be attributed to the presence of low formation energy sites within the HEA structure, which serve as strong traps for He, thereby restricting its migration. Since the migration barrier in W-based HEAs is considerably higher than that in pure W, it appears that He atoms are more likely to settle into relatively stable sites, which can then serve as nucleation points for fine bubbles, promoting the nucleation process [13]. Another potential mechanism is that as the irradiation dose increases, the radiation-induced or radiation-enhanced compositional fluctuations might cause local elemental segregation or even clustering. This chemical inhomogeneity could act as localized sinks for helium bubbles, creating preferential nucleation sites for helium atoms [33][34].

4.2 Evolution of dislocation loops

4.2.1 Dislocation loop mechanisms (literature)

Under the four irradiation conditions, small dislocation loops with the size of several nanometers were formed in WTaVCr HEA. The dislocation loops appeared to be randomly distributed within the foil, with no observable raft. This indicates that W-based HEA exhibits excellent resistance to loop formation under heavy ion irradiation, while pure W and conventional W alloys are prone to the formation of loop rafting [35]. At the same temperature, the size of the dislocation loop changes significantly, higher-dose irradiation may increase the number of loops but does not affect their size. This is because the significant lattice distortion in HEAs creates barriers to the movement of point defects [36]. Also, Yi et al. [37] conducted a comprehensive study on radiation damage generation and microstructure evolution of pure W and W-5 wt.% (Re, Ta) alloy was prepared by in-situ irradiation of 150 keV W^+ ion. The results indicate that alloying elements such as Re and Ta increased loop densities, which tended to reach saturation early in the irradiation process and subsequently restricted loop growth, which is consistent with our findings.

Much has been reported about the evolution of the dislocation loop Burger vector of ion irradiation W. Yi et al. [38] extended the irradiation temperature range to 773 K using 150 keV W^+ ions at a constant dose of approximately 10^{16} ions/m^2. The visible defect yields were as low as around 1%, with an average loop size of approximately 3.45 nm. Both ½ <111> and <100> loops were identified. In a separate study, it was observed that pure-edge ½ <111> configurations were the most thermally favored loop geometry, with nearly all loops being of this type at 1073 K [37]. Additionally, alloying influenced the relative thermal stability of ½ <111> and <100> loops. A higher proportion of <100> loops was observed in W-5Ta alloys compared to pure W. However, for WTaVCr, a more complex four-element alloy, the variation of the Burgess vector with temperature is rarely reported.

Fig. 5 shows the distribution of the damage peak region <100> loops of WTaVCr HEAs at different temperatures and He concentration. It is more obvious that with the increase of temperature, and the proportions corresponding to 500/800℃-7.5 × 10^{16} ions/cm^2 and 500/800℃-3.2 × 10^{17} ions/cm^2 are 14.8%, 21.6%, 20.5% and 24.3%, respectively. The formation energies for ½ <111> and <100> dislocation loops in tungsten are 9.55 and 11.49 eV, respectively [39][40]. This suggests that dislocation loops with $\boldsymbol{b}$ = ½ <111> are the most likely to form, as they have the lowest formation energy, whereas $\boldsymbol{b}$ = <100> loops are less favorable. Consequently, to promote the formation of $\boldsymbol{b}$ = <100> loops from the reaction of two $\boldsymbol{b}$ = ½ <111> loop variants, external driving forces such as higher irradiation temperatures, increased collision cascades, or extended irradiation times are required. High-density He clusters also influence the formation of loops. Yang et al. [41] demonstrated through MD simulations that the pressure field generated by He clusters facilitated the formation and growth of <100> loops in α-Fe. This implies that the presence and formation of <100> loops in He-irradiated tungsten could be due to the accumulation of high-density He. El-Atwani et al. [42] observed that dislocation loops created by He^+ irradiation in W exhibit high mobility. They further proposed that the formation of

<100> loops from ½ <111> loops is a plausible mechanism under low-energy He^+ irradiation. Li et al. [43] suggested that prolonged and elevated-temperature He^+ irradiation could serve as an external driving force for the reaction between two ½ <111> loop variants, leading to the formation of a <100> loop. Furthermore, 270 keV He^+ irradiation not only generates isolated Frenkel pair damage in materials but also induces extensive collision cascade damage in this study. The <100> loops may also form from dense cascades induced by heavy ions. Setyawan et al. [44] conducted displacement cascade simulations in tungsten and observed that <100> loops can directly form at high primary knock-on atom (PKA) energies, albeit with a relatively low probability.

The evolution of defect morphology is closely related to temperature. The stability of <100> loops with respect to <111> loops is highly temperature dependent. Dudarev et al. [45] theoretically demonstrated that the stability of <100> and ½<111> dislocation loops is strongly influenced by temperature, providing insight into experimental findings that show a decrease in the fractional population of ½<111> loops as temperature increases in Fe. Monte Carlo simulations by Xu et al. [46] on the coalescence of ½<111> dislocation loops revealed that new <100> dislocation loops can form through this process. The occurrence of such loop formation is closely tied to the frequency of loop coalescence, which is in turn influenced by factors such as dose, dose rate, temperature, alloy composition, and impurity content. Li et al. [43] observed both 1/2<111> and <100> type loops in tungsten foils irradiated in situ with 30 keV He^+ ions at varying irradiation temperatures. Statistical analysis revealed that, at 723 K, 88.3% of the loops were of the 1/2 <111> type, while 11.7% were <100> loops. At higher irradiation temperatures, the proportion of <100> loops increased, reaching 14.2% at 873 K and 19.4% at 973 K. This suggests that elevated irradiation temperatures promote the formation of <100> loops, which is similar with our research. They suggested that prolonged and elevated-temperature He^+ irradiation could serve as an external driving force for the reaction between two ½ <111> loop variants, leading to the formation of <100> loop. Liu et al. [47] observed that loops were observed to escape to the surface and disappeared, mobile ½ <111> should be the dominant type based on the fact that only at 573 K. At 673 K, the ratio of ½ <111> to <100> loop is around 1.02. At 773 K, the loops were found to be predominantly <100> type. They deduced that the <111> loops are highly mobile, whereas the <111> loops are sessile. Consequently, <111> loops can migrate over extended distances and interact with distant, pre-existing defects, thereby promoting the formation of dislocation segments and network dislocations at lower doses. In contrast, once formed, <100> loops serve solely as stationary defect sinks. Yao et al. [48] performed Fe^+ self-ion irradiation on pure Fe and reported that about 80% of the loops were of the <100> type at 673 K, which provided further evidence that <100> loops become increasingly dominant with increasing irradiation temperature. They proposed that at temperatures exceeding 450°C, the formation of small ½ <111> loops becomed less probable, and those that do form are rapidly absorbed into <100> loops, preventing them from growing to significant sizes. Above 500°C, this process may occur so swiftly that no microscopic ½ <111> loops form at all, resulting in the absence of

such loops in the high-temperature regime.

Similarly, the proportion of ½ <111> loops increased with rising irradiation temperature in pure W. Gilbert [49] attributed this trend to changes in free energy, observing that although the free energy for both ½ <111> and <100> loops in pure W rises with temperature, it increases at a significantly slower rate for ½ <111> loops. Additionally, the presence of solute atoms affected loop morphologies, for example Ta element can reduce the thermodynamic advantage of a ½ <111> loops [37], resulting in a higher proportion of <100> loops in the alloy than pure W. Schäublin et al. [50] found that the presence of Cr in FeCr alloys enhances the probability of <100> type loop formation at low doses (0.05 dpa), a condition where the interaction of <111> loops is improbable. This phenomenon may be attributed to the incorporation of Cr in the damage region following the thermal spike of the cascade.

4.2.2 Dislocation loop mechanisms (this work)

In order to determine the cause of the formation of dislocation loops, we investigated the chemical stability of the elements surrounding the dislocation loops. Atomic-scale irradiation-induced segregation at dislocation loops was investigated utilizing aberration-corrected scanning transmission electron microscopy coupled with energy-dispersive X-ray spectroscopy (STEM-EDS). Fig. 7 presents the atomic-resolution STEM-HAADF images of the dislocation loop observed in unirradiated and the sample after irradiation to a fluence of 3.2 × 1017 ions/cm2 under the imaging conditions (Z = [110] zone axis, and under strong two-beam conditions close to the [110] zone axis), along with corresponding EDS maps of element distributions. The symbol “T” denotes the inserted half-atomic planes. To enhance spatial resolution, high-resolution EDS acquisition was performed within the white-framed region.

Fig. 7(a) displays the morphology and elemental distribution in the unirradiated region, showing no detectable elemental aggregation. In contrast, Fig. 7(c) and 7(d) reveal that within irradiation-induced dislocation loop-dense zones, EDS analysis identifies noticeable Cr enrichment and Ta depletion around these loops. To further substantiate these findings, a comparative analysis of elemental distributions was conducted between regions containing dislocation loops (b2) and loop-free regions (b3) within Fig. 7(b1). The results consistently demonstrate distinct distribution patterns of Cr and Ta between the two regions, confirming the correlation between dislocation loops and solute segregation.

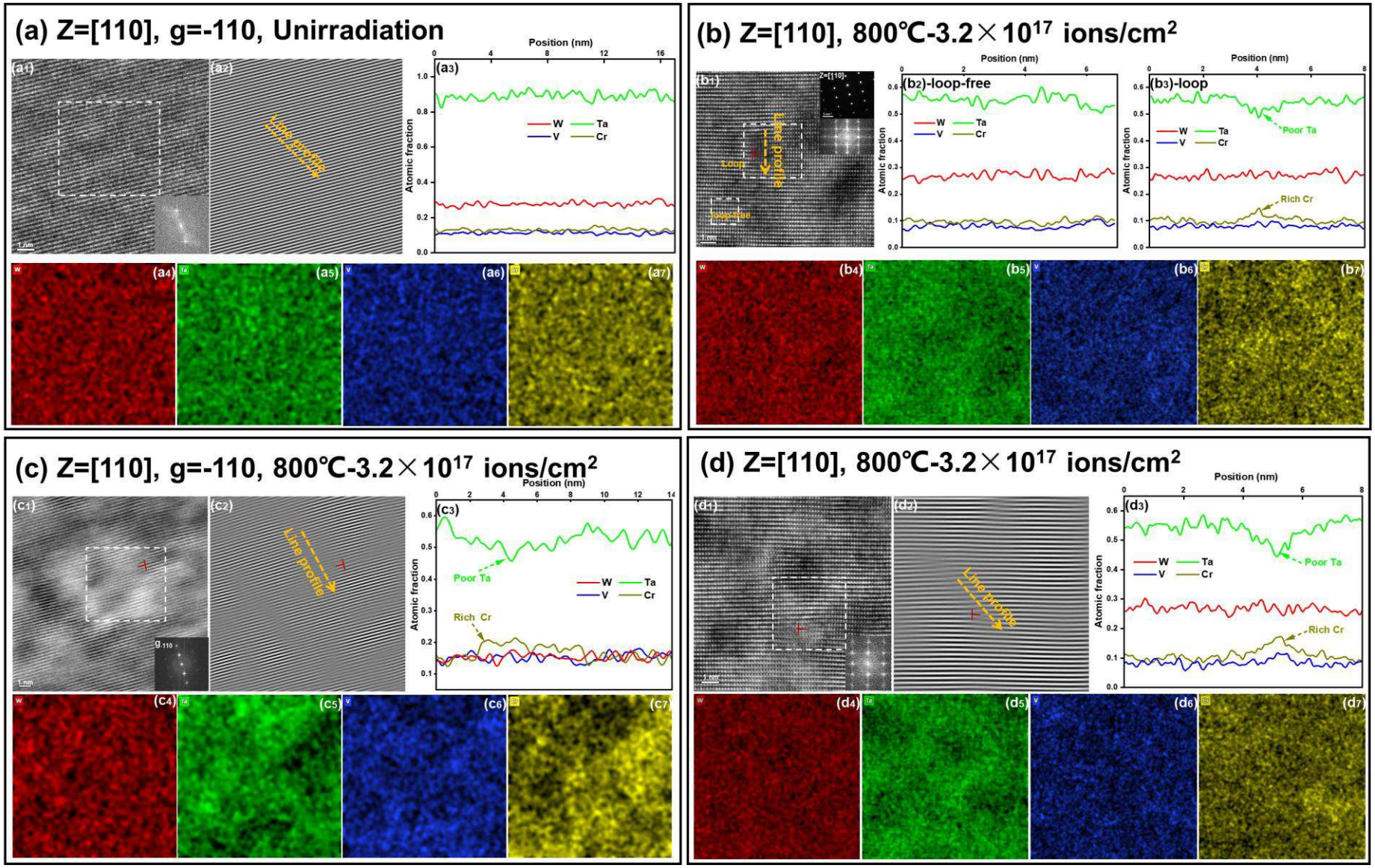

(a) Z=[110], g=-110, Unirradiation
(a1)
(a2)
Line profile
(a3)
Position (nm)
Atomic fraction
W
Ta
V
Cr
(a4)
(a5)
(a6)
(a7)
(b) Z=[110], 800℃-3.2×10^17 ions/cm^2
(b1)
Z=[110]
Line profile
Loop
Loop-free
(b2)-loop-free
(b3)-loop
Poor Ta
Rich Cr
(b4)
(b5)
(b6)
(b7)
(c) Z=[110], g=-110, 800℃-3.2×10^17 ions/cm^2
(c1)
(c2)
Line profile
(c3)
Poor Ta
Rich Cr
(c4)
(c5)
(c6)
(c7)
(d) Z=[110], 800℃-3.2×10^17 ions/cm^2
(d1)
(d2)
Line profile
(d3)
Poor Ta
Rich Cr
(d4)
(d5)
(d6)
(d7)

Fig. 7 Atomic-resolution STEM-HAADF images of the unirradiated region in (a) and (b-d) sample after He-irradiation fluence to 3.2×10^{17} ions/cm^2. The images of (a) and (c) were taken under strong two-beam conditions close to the [110] zone axis, and the corresponding diffraction vector is g=-110. EDS mapping of element distributions in the (a4)-(a7) unirradiated region, (b4)-(b7), (c4)-(c7) and (d4)-(d7) dislocation loop; (a2),(c2) and (d2) represent the IFFT within the white box in (a1),(c1) and (d1); (a3)-(d3) are line profiles of atomic fraction of individual elements taken from the respective EDS maps; the positions of the corresponding scan lines are respectively indicated by orange arrows. (b2) and (b3) correspond to the loop and loop-free regions in (b1) respectively.

To elucidate the atomic-scale mechanism of solute redistribution near dislocation loops in the WTaVCr HEA, we performed atomic-scale simulations using the LAMMPS software [51], and systematically analyzed the interactions between Cr and Ta elements with <100> and 1/2<111> dislocation loops (DL). For the atomic interactions in WTaVCr, the EAM potential was employed [52]. As shown in Fig. 8(a-d), a 12×12×12 BCC supercells with random atomic occupations were to simulate the chemical disorder characteristic of the high-entropy alloy. The concentration of W, Ta, V and Cr are 34%, 29%, 21% and 16%, respectively. In the dislocation-containing crystal models, the concentrations of W and V were kept constant, while the local concentrations of Ta and Cr near the dislocation sites were intentionally varied. Statistical averages were obtained by calculating the energies of 200 different atomic configurations. The formation energy was evaluated using the following expression:

$$E_f = iN[E_{loop}W_xTa_yV_zCr_{1-x-y-z} - EW_xTa_yV_zCr_{1-x-y-z}]N \quad (2)$$

In Eq.(2), $[E_{loop}W_xTa_yV_zCr_{1-x-y-z}$ is the total energy of the supercell with a the dislocation loop inside. $EW_xTa_yV_zCr_{1-x-y-z}$ is the total energy of the supercell with the same concentration.

Fig. 8(e) shows the formation energy of both <100> and 1/2<111> DLs as a function of the Cr concentration within the loops. For 1/2<111> dislocation loops, enrichment of Cr atoms substantially reduces the total formation energy of the system. This indicates a net attractive interaction between Cr and the dislocation, which energetically drives the spontaneous segregation of Cr toward the dislocation defects, whereas Ta does not favor residing near dislocations. For <100> dislocation loops, the formation energy is higher than that of the 1/2<111> loops, which agrees with experimental observations. Notably, when the Cr concentration at the dislocation loop reaches about 18%, the energy difference between the formation energies of the <100> and 1/2<111> loops is 15.8 eV. Moreover, the formation energy of <100> dislocation loops decreases with increasing Cr concentration in the loops, a trend similar to that observed for the 1/2<111> loops. As the Cr concentration gradually increases, the energy difference between the two types of DLs gradually decreases, suggesting a greater tendency for <100> DL formation. This is consistent with the experimental observation of a higher density of <100> dislocation loops.

The atomic radii of the four constituent elements-W, Ta, V, and Cr-follow the decreasing order: Ta (146 pm) > W (139 pm) > V (134 pm) > Cr (128 pm). When Cr, which possesses the smallest atomic radius, occupies the dislocation region, the resulting additional elastic strain energy of the system is minimized, making this configuration energetically most favorable from an elastic strain perspective. The observed reduction in total system energy upon Cr enrichment directly corroborates

this effect. Conversely, the introduction of Ta-the largest atom—into the dislocation core would introduce substantial elastic strain, significantly raising the overall strain energy of the system. To further quantify this trend, we calculated the local pressure across different atomic configurations (as shown in Fig.8 (f-g). From the figure, we can see that, the number of atoms with large atomic pressure is greatly decreased. Specially, for the 1/2<111> DL, the average absolute atomic pressure in the supercell is 9.98×10^5 bar*Å3 when the Cr concentration is 18%. As the Cr concentration within the loop increases to 45.9%, the average absolute local pressure drops to 9.86×10^5 bar*Å3, corresponding to a reduction of about 1.2%. Hence, the incorporation of Cr atoms into the dislocation loop effectively relieves the local atomic pressure. From the viewpoint of atomic size effects, the segregation of Cr toward DL represents a spontaneous process driven by strain-energy relaxation, whereas the depletion of Ta near dislocations serves to avoid high strain-energy penalties.

Through systematic configurational averaging calculations, this work reveals the physical origin of the selective interaction between solutes and dislocations in the WTaVCr HEA from an energy standpoint: the segregation of Cr is a thermodynamically driven spontaneous process. This not only provides a reasonable explanation for existing experimental observations but also offers a theoretical basis for tailoring defect behavior and mechanical properties in HEAs through compositional design.

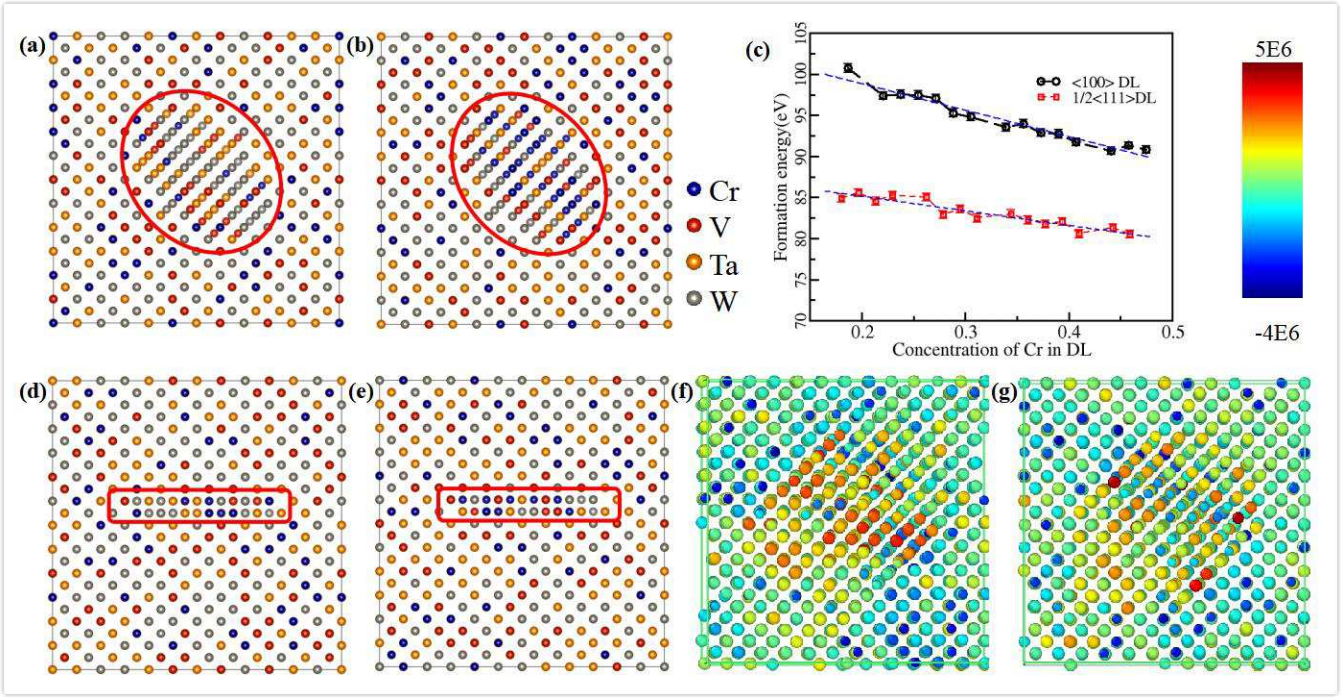


Fig.8 The structures of 1/2<111> dislocation loops (DLs) are shown for local Cr concentrations of (a) 18% and (b) 46%. The corresponding structures of ⟨100⟩ DLs are presented for Cr concentrations of (c) 18.6% and (d) 47.4%. (e) Formation energies of <100> and 1/2<111> DLs as a function of the local Cr concentration within the loop. Atomic pressure distribution in the supercell containing a 1/2<111> DL is displayed for local Cr concentrations of (f) 18% and (g) 46%.

4.3 Radiation hardening

Hardening introduced by irradiation in metallic materials is largely due to the obstruction of dislocation motion by defect clusters [53]. Dislocation loops and bubbles serve as barriers to dislocation movement, resulting in an increased yield stress ($\Delta\sigma_y$). This increase in yield stress caused by irradiation-induced defects can be quantified using the following equation based on the dispersed barrier hardening (DBH) model [54][55].

$$\Delta\sigma_y = M\alpha\mu b\sqrt{Nd} \tag{3}$$

$$\Delta H = K\Delta\sigma_y \tag{4}$$

$$\Delta\sigma_{Total} = \sqrt{\sigma_{He}{}^2 + \sigma_{Loop}{}^2} \tag{5}$$

where M is the Taylor factor (3.06 for BCC alloys) [56], α is the barrier strength dependence factor (0.2 for He bubbles, 0.173 for <111> loops and 0.545 for <100> loops in BCC materials [57]), μ is the shear modulus (270 GPa for WTaVCr) [58], $\boldsymbol{b}$ is the Burgers vector (0.2741 nm), N is the defect number density, and d is the average diameter of irradiation defects. Busby [59] analyzed experimental data on irradiated austenitic and ferritic stainless steels, determining that the best-fit values of k were 3.23 for austenitic steels and 3.20 for ferritic steels. Due to the theoretical model's simplifications, this study utilizes the experimentally derived linear coefficient. Consequently, the relationship ΔH=3.2 σ_y is applied, appropriate for the BCC lattice structures of both tungsten and ferritic stainless steels. The ultimate formula for predicting the hardening contribution, based on the measured defect density, size, and type, is

$$\Delta H = 3.20M\alpha\mu b\sqrt{Nd} \tag{6}$$

Table 1 illustrates the hardening outcomes based on the statistical analysis of irradiation defects and He bubbles in the irradiated WTaVCr.

Table 1 Hardening predicted from the DBH model contributed by He bubbles and dislocation loops in the peak damage region.

Temperature (℃)	He fluence (10^{16} ions/cm^2)	Defects	N (10^{23}/m^3)	d (nm)	$\Delta\sigma_y$ (MPa)	$\Delta\sigma_{Loop}$ (MPa)	$\Delta\sigma_{Total}$ (MPa)	ΔH_{DBH} (GPa)	Ratio of <100> loops (%)
500	7.5	Bubbles	1.43	0.86	502.27	579.87	767.16	2.45	14.8
		Loop$_{<111>}$	1.14	1.14	395.58				
		Loop$_{<100>}$	0.90	1.27	423.98				
	32	Bubbles	2.04	0.96	633.83	716.13	954.34	3.06	21.6
		Loop$_{<111>}$	0.69	1.91	398.36				
		Loop$_{<100>}$	1.42	1.62	595.10				
800	7.5	Bubbles	1.06	1.02	470.95	642.09	796.29	2.55	20.5
		Loop$_{<111>}$	0.40	1.93	304.89				
		Loop$_{<100>}$	1.08	1.88	565.09				
	32	Bubbles	1.54	1.08	584.11	677.80	894.76	2.86	24.3
		Loop$_{<111>}$	0.38	2.88	363.01				
		Loop$_{<100>}$	1.12	1.86	572.39				

The irradiation hardening of materials mainly results from the hindering effect of irradiation-induced defects. It is worth noting that the hardening increment (ΔH_{DBH}) calculated based on the diffuse barrier hardening model is lower than the value obtained through the Nix-Gao model ($\Delta H_{Nix\text{-}Gao}$), mainly because in this study, when calculating the hardening induced by defects using ΔHDBH, only He bubbles and dislocation loops were considered, and no other types of defects were involved. Zheng et al. [60] believe that the ultra-high irradiation hardening observed in tungsten is due to the strong interaction between dislocations and the visible helium bubbles under transmission electron microscopy, as well as the atomic-scale hidden defects (especially vacancies and helium-vacancy complexes). Through the analysis of the distribution of atoms (helium ions), it was found that over 87% of vacancies and helium atoms are in a "hidden" state. A large number of helium-vacancy complexes are frozen in the lattice due to the high energy barrier for vacancy migration. Combined with in-situ nano-mechanical testing and atomic-scale calculations, they confirmed that the irradiation hardening mainly results from the high-density atomic-scale hidden point defect complexes. Moreover, the increment of irradiation hardening is mainly related to dislocation loops. In BCC materials, dislocation loops with the Burgers vector $\boldsymbol{b}$ = ½<111> usually have mobility, while dislocation loops with the vector $\boldsymbol{b}$ = <100> are relatively fixed [61][62]. Therefore, the former is more likely to migrate to defect traps such as grain boundaries or annihilate with other defects; conversely, immobile <100> dislocation loops tend to accumulate in the microstructure, leading to an increase in the number of immobile pinning points and further exacerbating the irradiation hardening and brittleness of the material. In this study, the irradiation hardening is mainly dominated by the combined effect of dislocation loop density, size, and the proportion of <100> type dislocation loops.

5. Conclusions

Our study reveals that chemical disorder in the WTaVCr high entropy alloy enables unprecedented control over helium induced defects, offering a radiation tolerance paradigm beyond conventional materials. Three key advances are highlighted:

Helium bubble self limitation: Bubble size remains stable under high dose irradiation, overcoming the pervasive coarsening seen in tungsten. This is attributed to low energy trapping sites and suppressed helium mobility within the disordered lattice.

Solute directed dislocation loop character: Atom-resolved analysis and simulations reveal Cr enrichment and concurrent Ta depletion at dislocation loops. The energetic preference for Cr arises from its net attractive interaction with the dislocation core, driving spontaneous solute segregation, while Ta is thermodynamically excluded. As Cr accumulates, the formation energy difference between 1/2<111> and <100> dislocation loops decrease, explaining the observed dominance of <100> loop formation in WTaVCr HEA. This chemically mediated strain relaxation-where chromium mitigates local lattice distortion while tantalum depletion avoids elastic penalty-establishes solute redistribution as an active driver of defect evolution in irradiated multicomponent alloys.

Predictable property evolution: Hardening is dominated by dislocation loops, with <100> loops acting as immobile obstacles. The dispersed-barrier hardening model aligns well with experimental data.

The WTaVCr HEA demonstrates that targeted chemical complexity can tailor defect formation, migration, and interaction-transforming radiation induced damage from a life limiting factor into a manageable phenomenon. This solute mediated defect engineering strategy opens a broad avenue for developing materials for fusion, fission, and advanced nuclear systems where extreme radiation tolerance is imperative.

Acknowledgement

This work was supported by the National Key R&D Program of China (Grant No. 2022YFE03030000), the National Natural Science Foundation of China (Grant Nos. 12575219, 12205349, 12205333), and the Anhui Provincial Natural Science Foundation (Grant No. 2208085J40). We also express our gratitude to Professor Shijun Zhao from City University of Hong Kong for sharing knowledge on the alloy potential function.

References

[1] I.P.B. Editors, Co-Chairs I P E G C, Unit I J C T P I. Chapter 1: Overview and summary[J]. Nucl. Fusion, 1999, 39(12): 2137-2174.

[2] V. Philipps. Tungsten as material for plasma-facing components in fusion devices[J]. J. Nucl. Mater., 2011, 415(1): S2-S9.

[3] J. Marian, C.S. Becquart, C. Domain, et al. Recent advances in computational

materials modeling of tungsten as plasma-facing material for fusion energy applications[J]. Nucl. Fusion, 2017, 57(9): 092008.
[4] F. Sefta, K.D. Hammond, N. Juslin, et al. Tungsten surface evolution by helium bubble nucleation, growth and rupture[J]. Nucl. Fusion, 2013, 53(7): 073015.
[5] M. Rieth, S.L. Dudarev, S.M.G. De Vicente, et al. Recent progress in research on tungsten materials for nuclear fusion applications in Europe[J]. J. Nucl. Mater., 2013, 432(1-3): 482-500.
[6] O. El-Atwani, S. Gonderman, S. Suslov, et al. Early stage damage of ultrafine-grained tungsten materials exposed to low energy helium ion irradiation[J]. Fusion Eng. Des., 2015, 93: 9-14.
[7] O. El-Atwani, A. Suslova, T.J. Novakowski, et al. In-situ TEM/heavy ion irradiation on ultrafine-and nanocrystalline-grained tungsten: Effect of 3 MeV Si, Cu and W ions[J]. Mater. Charact., 2015, 99: 68-76.
[8] D.B. Miracle, O.N. Senkov. A critical review of high entropy alloys and related concepts[J]. Acta Mater, 2017, 122: 448-511.
[9] S. Zhao. Defect properties in a VTaCrW equiatomic high entropy alloy (HEA) with the body centered cubic (bcc) structure[J]. J. Mater. Sci. Technol., 2020, 44: 133-139.
[10] S. Zhao, T. Egami, G.M. Stocks, et al. Effect of d electrons on defect properties in equiatomic NiCoCr and NiCoFeCr concentrated solid solution alloys[J]. Phys. Rev. Mater., 2018, 2(1): 013602.
[11] S. Zhao, Y. Osetsky, A.V. Barashev, et al. Frenkel defect recombination in Ni and Ni-containing concentrated solid–solution alloys[J]. Acta Mater., 2019, 173: 184-194.
[12] O. El-Atwani, N. Li, M. Li, et al. Outstanding radiation resistance of tungsten-based high-entropy alloys[J]. Sci. adv., 2019, 5(3): eaav2002.
[13] O. El-Atwani, A. Alvarado, K. Unal, et al. Helium implantation damage resistance in nanocrystalline W-Ta-V-Cr high entropy alloys[J]. Mater. Today Energy, 2021, 19: 100599.
[14] D. Kalita, I. Jóźwik, Kurpaska, et al. The microstructure and He+ ion irradiation behavior of novel low-activation W-Ta-Cr-V refractory high entropy alloy for nuclear applications[J]. Nucl. Mater. Energy, 2023, 37: 101513.
[15] R.E. Stoller, M.B. Toloczko, G.S. Was, et al. On the use of SRIM for computing radiation damage exposure[J]. Nucl. Instrum. Methods Phys. Res. Sect. B Beam Interact. Mater. Atoms, 2013, 310: 75-80.
[16] A.Y. Konobeyev, U. Fischer, Y.A. Korovin, et al. Evaluation of effective threshold displacement energies and other data required for the calculation of advanced atomic displacement cross-sections[J]. Nuclear Energy and Technology, 2017, 3(3): 169-175.
[17] Y. Li, M. Song, P. Zhu, et al. Flash electropolishing of BCC Fe and Fe-based alloys[J]. J. Nucl. Mater., 2023, 586: 154672.
[18] W.C. Oliver, G. M. Pharr. Measurement of hardness and elastic modulus by instrumented indentation: Advances in understanding and refinements to methodology[J]. J. Mater. Res., 2004, 19(1): 3-20.

[19] S. Li, Y. Wang, X. Dai, et al. Evaluation of hardening behaviors in ion-irradiated Fe-9Cr and Fe-20Cr alloys by nanoindentation technique, J. Nucl. Mater., 2016, 478: 50-55.
[20] R. Kasada, Y. Takayama, K. Yabuuchi, et al. A new approach to evaluate irradiation hardening of ion-irradiated ferritic alloys by nano-indentation techniques, Fusion Eng. Des., 2011, 86 (9-11): 2658-2661.
[21] W.D. Nix, H. Gao. Indentation size effects in crystalline materials: a law for strain gradient plasticity[J]. J. Mech. Phys. Solids, 1998, 46(3): 411-425.
[22] D.L. Plumton, W.G. Wolfer. Suppression of void nucleation by injected interstitials during heavy ion bombardment[J]. J. Nucl. Mater., 1984, 120(2-3): 245-253.
[23] F.A. Garner. Impact of the injected interstitial on the correlation of charged particle and neutron-induced radiation damage[J]. J. Nucl. Mater., 1983, 117: 177-197.
[24] J. Chai, D. Zhu, Z. Guo, et al. Microstructure evolution and hardening of helium ion irradiated tungsten[J]. Vacuum, 2025, 235: 114153.
[25] C. Fu, J. Li, J. Bai, et al. Effect of helium bubbles on irradiation hardening of additive manufacturing 316L stainless steel under high temperature He ions irradiation[J]. J. Nucl. Mater., 2021, 550: 152948.
[26] C. Becquart, C. Domain, Ab initio calculations about intrinsic point defects and He in W, Nucl. Instrum. Methods Phys. Res. Sect. B Beam Interact. Mater. Atoms, 255 (1) (2007) 23-26.
[27] P. Zhang, T. Zou, J. Zhao, He-He and He-metal interactions in transition metals from first-principles, J. Nucl. Mater., 467 (2015) 465-471.
[28] S.C. Lee, J.H. Choi, J.G. Lee, Energetics of He and H atoms with vacancies in tungsten: first-principles approach, J. Nucl. Mater., 383 (2009) 244-246.
[29] A. Samin, A physics-based machine learning study of the behavior of interstitial helium in single crystal W-Mo binary alloys, J. Appl. Phys., 127 (2020), 175904.
[30] Zhai Y X, Li Y H, Yang T R, et al. Weakening the self-trapping of helium by electron density regulation in WTaVCr high-entropy alloys[J]. Scripta Mater., 2024, 242: 115930.
[31] A. Seko, S.R. Nishitani, I. Tanaka, et al., First-principles calculation on free energy of precipitate nucleation, Calphad 28 (2004) 173-176.
[32] Y. Shi, Z. Jiang, T. Xia, et al., Helium diffusion and bubble evolution in single-phase tungsten-based W-Ta-Cr-V complex concentrated alloy, J. Nucl. Mater., 578 (2023), 154335.
[33] B. Mazumder, M.E. Bannister, F.W. Meyer, et al. Helium trapping in carbide precipitates in a tempered F82H ferritic–martensitic steel[J]. Nucl. Materi. Energy, 2015, 1: 8-12.
[34] W. Kesternich. Helium trapping at dislocations, precipitates and grain boundaries[J]. Radiation effects, 1983, 78(1-4): 261-273.
[35] O. El-Atwani, W. Cunningham, E. Esquivel, et al., In-situ irradiation tolerance investigation of high strength ultrafine tungsten-titanium carbide alloy, Acta Mater., 164 (2019) 547-559.
[36] Z. Zhang, E.H. Han, C. Xiang. Irradiation behaviors of two novel single-phase bcc-structure high-entropy alloys for accident-tolerant fuel cladding[J]. J. Mater.

Sci. Technol., 2021, 84: 230-238.
[37] X. Yi, M.L. Jenkins, M.A. Kirk, et al. In-situ TEM studies of 150 keV W+ ion irradiated W and W-alloys: Damage production and microstructural evolution[J]. Acta Mater., 2016, 112: 105-120.
[38] X. Yi, M.L. Jenkins, M. Briceno, S.G. Roberts, Z. Zhou, M.A. Kirk, In situ study of self-ion irradiation damage in W and W-5Re at 500 °C, Philos. Mag., 93 (2012) 1715-1738.
[39] D. Nguyen-Manh, A.P. Horsfield, S.L. Dudarev. Self-interstitial atom defects in bcc transition metals: Group-specific trends[J]. Physical Review B-Condensed Matter and Materials Physics, 2006, 73(2): 020101.
[40] D. Nguyen-Manh, S.L. Dudarev, A.P. Horsfield. Systematic group-specific trends for point defects in bcc transition metals: an ab initio study[J]. J. Nucl. Mater., 2007, 367: 257-262.
[41] L. Yang, H. Liu, H.L. Zhou, et al. Enhanced formation of <100> and <111> interstitial loops by helium clustering in bcc iron[J]. Mater. Lett., 2017, 190: 260-262.
[42] O. El-Atwani, W.S. Cunningham, J.R. Trelewicz, et al. Revealing the synergistic effects of sequential and simultaneous dual beam irradiations in tungsten via in-situ TEM[J]. J. Nucl. Mater., 2020, 538: 152150.
[43] Y. Li, L. Wang, G. Ran, et al. In-situ TEM investigation of 30 keV He^+ irradiated tungsten: Effects of temperature, fluence, and sample thickness on dislocation loop evolution[J]. Acta Mater., 2021, 206: 116618.
[44] W. Setyawan, G. Nandipati, K.J. Roche, et al. Displacement cascades and defects annealing in tungsten, Part I: Defect database from molecular dynamics simulations[J]. J. Nucl. Mater., 2015, 462: 329-337.
[45] S.L. Dudarev, R. Bullough, P.M. Derlet. Effect of the α-γ phase transition on the stability of dislocation loops in bcc iron[J]. Phys. Rev. Lett., 2008, 100(13): 135503.
[46] H. Xu, R.E. Stoller, Y.N. Osetsky, et al. Solving the puzzle of <100> interstitial loop formation in bcc iron [J]. Phys. Rev. Lett., 2013, 110(26): 265503.
[47] X. Liu, Y. Miao, M. Li, et al. Ion-irradiation-induced microstructural modifications in ferritic/martensitic steel T91[J]. J. Nucl. Mater., 2017, 490: 305-316.
[48] Z. Yao, M.L. Jenkins, M. Hernández-Mayoral, et al. The temperature dependence of heavy-ion damage in iron: A microstructural transition at elevated temperatures [J]. Philos. Mag., 2010, 90(35-36): 4623-4634.
[49] M.R. Gilbert, Private communication, Curr. Opin. Solid State Mater. Sci 19 (2015) 277-286.
[50] R. Schäublin, B. Décamps, A. Prokhodtseva, et al. On the origin of primary ½ a0< 111> and a0<100> loops in irradiated Fe (Cr) alloys[J]. Acta Mater., 2017, 133: 427-439.
[51] A.P. Thompson, H.M. Aktulga, R. Berger, et al. LAMMPS-a flexible simulation tool for particle-based materials modeling at the atomic, meso, and continuum scales[J]. Comput. Phys. Commun., 2022, 271: 108171.

[52] X.W. Zhou, R.A. Johnson, H.N.G. Wadley, Misfit-energy-increasing dislocations in vapor-deposited CoFe/NiFe multilayers. Phys. Rev. B, 2004. 69(14): p. 144113.
[53] B.N. Singh, A.J.E. Foreman, H. Trinkaus. Radiation hardening revisited: role of intracascade clustering[J]. J. Nucl. Mater., 1997, 249(2-3): 103-115.
[54] S. Jiang, C. Yu, P. Zheng, et al. Bubbles and precipitates formation and effects on the hardening of irradiated vanadium alloys, J. Nucl. Mater., 544 (2021) 152712.
[55] J. Gan, G.S. Was. Microstructure evolution in austenitic Fe-Cr-Ni alloys irradiated with rotons: comparison with neutron-irradiated microstructures[J]. J. Nucl. Mater., 2001, 297(2): 161-175.
[56] X. Hu, T. Koyanagi, M. Fukuda, et al. Irradiation hardening of pure tungsten exposed to neutron irradiation[J]. J. Nucl. Mater., 2016, 480: 235-243.
[57] J. Gao, K. Yabuuchi, A. Kimura. Ion-irradiation hardening and microstructural evolution in F82H and ferritic alloys[J]. J. Nucl. Mater., 2019, 515: 294-302.
[58] H. Luo, B. Long, S. Lu, et al. Dislocation loops, segregation and hardening induced by high-dose ion irradiation of NbMoTaW and VCrTaW high-entropy alloy coatings on the T91 substrate[J]. Surf. Coat. Tech., 2023, 473: 130019.
[59] J.T. Busby, M.C. Hash, G.S. Was. The relationship between hardness and yield stress in irradiated austenitic and ferritic steels[J]. J. Nucl. Mater., 2005, 336(2-3): 267-278.
[60] R.Y. Zheng, W.R. Jian, I.J. Beyerlein, et al. Atomic-scale hidden point-defect complexes induce ultrahigh-irradiation hardening in tungsten [J]. Nano Letters, 2021, 21(13): 5798-5804.
[61] R.W. Harrison, J.A. Hinks, S.E. Donnelly. Influence of pre-implanted helium on dislocation loop type in tungsten under self-ion irradiation[J]. Scripta Mater., 2018, 150: 61-65.
[62] A. Prokhodtseva, B. Décamps, A. Ramar, et al. Impact of He and Cr on defect accumulation in ion-irradiated ultrahigh-purity Fe (Cr) alloys[J]. Acta Mater., 2013, 61(18): 6958-6971.

Supplementary Files

This is a list of supplementary files associated with this preprint. Click to download.

- GraphicalAbstract.pdf